Eric Climent
Laboratoire de Génie Chimique,
UMR 5503,
CNRS/INPT/UPS,
5 Rue Paulin Talabot,
31106 Toulouse, France
e-mail: eric.climent@ensiacet.fr

Kyongmin Yeo
e-mail: kyeo@dam.brown.edu

Martin R. Maxey
e-mail: maxey@dam.brown.edu

George E. Karniadakis
e-mail: gk@dam.brown.edu

Center for Fluid Mechanics,
Division of Applied Mathematics,
Brown University,
Box F,
Providence, RI 02912

Dynamic Self-Assembly of Spinning Particles

This paper presents a numerical study of the dynamic self-assembly of neutrally buoyant particles rotating in a plane in a viscous fluid. The particles experience simultaneously a magnetic torque that drives their individual spinning motion, a magnetic attraction toward the center of the domain, and flow-induced interactions. A hydrodynamic repulsion balances the centripetal attraction of the magnetized particles and leads to the formation of an aggregate of several particles that rotates with a precession velocity related to the inter-particle distance. This dynamic self-assembly is stable (but not stationary) and the morphology depends on the number of particles. The repulsion force between the particles is shown to be the result of the secondary flow generated by each particle at low but nonzero Reynolds number. Comparisons are made with analogous experiments of spinning disks at a liquid–air interface, where it is found that the variation in the characteristic scales of the aggregate with the rotation rate of individual particles are consistent with the numerical results. [DOI: 10.1115/1.2436587]

Keywords: magnetic particles, rotating aggregate, hydrodynamic interactions, direct simulation

1 Introduction

Flows in microsystems have received increasing attention over the past decade because of the broad range of potential applications, as described in the review paper of Stone et al. [1]. Microdevices can be used for multiple purposes ranging from biomedicine (drug delivery, molecular diagnostic using Lab-On-Chip equipment) to the transport of fluids in aerospace engineering [2]. Microfabrication techniques primarily developed for microelectronics provide a convenient way to achieve channels with complex geometries and also surface patterning. Both academic research and engineering applications [2] have revealed the particular behavior of flows in very confined geometries. It is now possible to control more efficiently the basic transport phenomena (heat and mass) that drive the overall performance of the system. Mixing in such small-scale devices [3] is a challenge as turbulence is generally absent at the low Reynolds numbers encountered in flows in these systems. Different strategies, ranging from passive to dynamically enhanced mixing [4,5], have been proposed to overcome these limitations. Manipulating the flow with actuators or internal micropumps is another important issue. One way to achieve this is through the organized motion of particles in a controllable manner. For example, experiments by Terray et al. [6] have demonstrated the peristaltic pumping action produced by a transverse wave traveling along a chain of micron scale beads. Numerical simulations [7] confirm the basic flow features and provide additional information including the effects of different channel sizes. The application of magnetic fields to magnetic or paramagnetic beads provides a valuable means to drive the particle motion. Magnetic fields, in general, are more benign for handling biological samples and do not require large electrostatic potentials encountered in flows driven by electro-osmosis.

Recently, there has been a focus on fabricating self-assembled structures using paramagnetic particles suspended by liquids in microchannels [8,9]. In an open suspension, at void fractions of a few percent or less, magnetic beads form linear chains under the action of a steady magnetic field. The beads acquire a magnetic dipole parallel to the applied field and then align themselves in response to the mutual interaction of the dipoles, forming long chains through aggregation. For micron-sized particles, there are competing effects of Brownian motion and magnetic forces and the average length of the chains has a power law growth in time [10,11]. In a confined microchannel, the length and position of the chains is controlled by the geometry. Experiments by Hayes et al. [8] show that paramagnetic particles suspended in a pipe will form a chain along a diameter of the pipe when a transverse magnetic field is applied. This represents the longest available dimension parallel to the applied field. The chain, once formed, will then rotate as the magnetic field is rotated, maintaining the alignment of the chain with the magnetic field. Corresponding numerical simulations by Liu et al. [12] confirm this behavior and show similar preferred alignments of paramagnetic chains in ducts with a triangular cross section. Self-assembled matrices of paramagnetic particles in a microchannel have been proposed for DNA separation chips [9].

Self-assembly is a specific form of particle manipulation. Autonomous organization can spontaneously lead to the formation of large-scale structures and through the balance of opposing forces or processes, particles can form stable patterns. This behavior is common to several systems ranging from molecular to planetary scales [13]. Studies of self-organization have been mainly focused on static structures, such as crystal formation, where a static equilibrium is achieved through an energy minimization. In contrast, a stable particle aggregate that is moving in a viscous fluid is continuously dissipating energy and a dynamic equilibrium between the external forcing and the viscous dissipation is needed to maintain the self-assembled pattern. This represents, in general, a dissipative dynamical system rather than a conservative system governed by Hamiltonian dynamics.

The present paper is motivated by the experiments reported by Grzybowski et al. [14–16] in which the self-assembling system is composed of millimeter-sized disks floating just beneath a liquid–air interface. These disks are doped with magnetite resulting in magnetized particles with a permanent dipole moment coplanar with the disk. A large permanent bar magnet rotates at a constant angular frequency above the interface in a plane parallel to the interface. The disks spin about their centers at the same rotation

Contributed by the Fluids Engineering Division of ASME for publication in the JOURNAL OF FLUIDS ENGINEERING. Manuscript received May 24, 2006; final manuscript received October 18, 2006. Assoc. Editor: Theodore Heindel.

 Copyright © 2007 by ASME

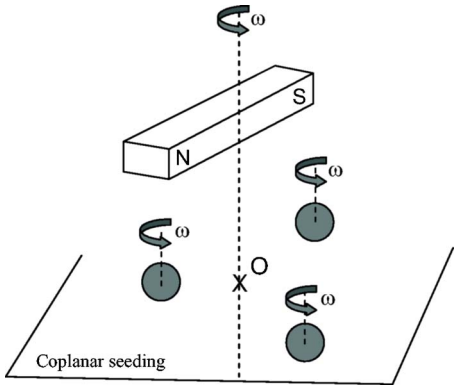

Fig. 1 Sketch of the experimental configuration [15]

rate as the rotating bar magnet in response to the magnetic torque on the disks. The particles experience also a gradient of the mean magnetic field resulting in a centripetal force toward the axis of rotation of the bar magnet. As the disks are rotating in a viscous fluid, they force the formation of a vortex like flow around their surfaces. Complex hydrodynamic interactions between the spinning disks then take place and drive the formation of supraparticle aggregates.

By comparison, the interactions of these vortical flows differ from the motion of two-dimensional point vortices in an inviscid fluid described by Aref [17]. In the latter case, the system is Hamiltonian and nondissipative. The dynamics can be complex and chaotic motions may occur depending on the number of vortices and the initial separation distance of the vortex centers. Similarly, Campbell and Ziff [18] have investigated theoretically the possible equilibrium patterns formed by point vortices in an inviscid superfluid using energy minimization principles. In the present study, viscous forces and viscous dissipation play a central role in damping fluctuations and sustaining the stable dynamic equilibrium.

The aim of this paper is to present results of numerical simulations for an analog of the physical situation described by Grzybowski et al. [15,16]. The floating disks are instead neutrally buoyant spheres, suspended in a viscous liquid and initially seeded in a coplanar configuration (see Fig. 1). A constant torque is applied to each particle to generate their spinning motion and the centripetal attraction force due to the radial gradient of the ambient magnetic field is prescribed. In the following sections, we describe the numerical approach used to simulate the flow and particle trajectories, giving details of the force coupling method. The flow around individual spinning particles is described and the hydrodynamic interactions of the particles evaluated. Then, we describe the results obtained from simulations of systems of particles and compare these carefully with the experimental data [15]. We emphasize the effect of the low but finite Reynolds number on the flow dynamics. This point is particularly important as the Reynolds number is of order unity in the experiments and no reliable analytical theory is available for such an intermediate regime.

2 Simulation methods

The physical problem under discussion involves magnetic attraction forces and torques as well as fluid forces induced by the rotation of small particles embedded in a viscous fluid. The crucial mechanism that needs to be represented is the repulsion force between spinning particles produced by their hydrodynamic interactions. We use the force coupling method (FCM) [19,20] to describe the coupled dynamics of the dispersed two-phase flow of the particles in suspension. The resulting equations are solved numerically, in a three-dimensional periodic domain using a standard Fourier pseudo-spectral method.

2.1 Overview of the Force Coupling Method. The basic concept of the FCM is to represent the presence of particles in a fluid flow by locally distributed body forces added to the Navier–Stokes equations for the fluid momentum. Fluid is assumed to fill the whole domain including the volume occupied by the particles. The body forces result in a low-order, finite multipole expansion for the disturbance flow of each particle and the forces effectively constrain the fluid to respond locally as a rigid body. Multibody interactions are achieved by solving the Navier–Stokes Eqs. (1) and (2) including simultaneously the forcing $\mathbf{f}(\mathbf{x},t)$ from all the particles

$$\rho\frac{D\mathbf{u}}{Dt} = -\nabla p + \mu\nabla^2\mathbf{u} + \mathbf{f}(\mathbf{x},t) \tag{1}$$

The velocity field is $\mathbf{u}(\mathbf{x},t)$; μ is the fluid viscosity; and p is the pressure. The fluid motion is incompressible, with uniform density ρ, and the velocity field satisfies the continuity equation

$$\nabla\cdot\mathbf{u} = 0 \tag{2}$$

The momentum source term $\mathbf{f}(\mathbf{x},t)$ on the right-hand side of Eq. (1) is expanded using a multipole decomposition

$$f_i(\mathbf{x},t) = \sum_{n=1}^{N_B} F_i^{(n)}\Delta[\mathbf{x}-\mathbf{Y}^{(n)}(t)] + G_{ij}^{(n)}\frac{\partial}{\partial x_j}\Delta'[\mathbf{x}-\mathbf{Y}^{(n)}(t)] \tag{3}$$

where $\mathbf{Y}^{(n)}$ is the position of the nth spherical particle and $\mathbf{F}^{(n)}$ is the force it exerts on the fluid. The first term on the right-hand side of Eq. (3) is a force monopole. The force dipole term, the second term on right-hand side of Eq. (3), is a combination of a symmetric stresslet term and an antisymmetric part related to the torque $\mathbf{T}^{(n)}$ exerted on the fluid by the nth particle. These terms are summed over the total number of particles, N_B. The density functions Δ and Δ' are spherical Gaussian envelopes that model the finite size of the particles

$$\Delta(\mathbf{x}) = (2\pi\sigma^2)^{-3/2}\exp(-\mathbf{x}^2/2\sigma^2) \tag{4}$$

with corresponding length scales σ for $\Delta(\mathbf{x})$ and σ' for $\Delta'(\mathbf{x})$. In terms of the particle radius a, these scales are set as $a/\sigma=\sqrt{\pi}$ and $a/\sigma'=(6\sqrt{\pi})^{1/3}$.

The strength of each force monopole $\mathbf{F}^{(n)}$ is related to the external force on the particle $\mathbf{F}_{\text{ext}}^{(n)}$ and the excess buoyancy force or inertia of the particle relative to that of the displaced fluid as

$$\mathbf{F}^{(n)} = (m_P - m_F)\left(\mathbf{g} - \frac{d\mathbf{V}^{(n)}}{dt}\right) + \mathbf{F}_{\text{ext}}^{(n)} \tag{5}$$

Similarly, the torque term $\mathbf{T}^{(n)}$ is specified by a combination of the external torque on the particle and excess inertia

$$\mathbf{T}^{(n)} = -(I_P - I_f)\left(\frac{d\boldsymbol{\omega}^{(n)}}{dt}\right) + \mathbf{T}_{\text{ext}}^{(n)} \tag{6}$$

Here, m_P and m_F are the mass of the particle and mass of displaced fluid, respectively; and I_P and I_F are appropriate coefficients for the moment of inertia. The contribution of the torque term to the force dipole coefficient is $G_{ij}^{(n)}=1/2\varepsilon_{ijk}T_k^{(n)}$. In general, the symmetric stresslet coefficient for each particle is set through an iteration process to ensure that the average rate of strain within the volume occupied by each particle

$$S_{ij}^{(n)} = \frac{1}{2}\int\left(\frac{\partial u_i}{\partial x_j} + \frac{\partial u_j}{\partial x_i}\right)\Delta'[\mathbf{x}-\mathbf{Y}^{(n)}(t)]d^3\mathbf{x} \tag{7}$$

is zero.

The particles move in a Lagrangian framework with their trajectories computed from the local fluid velocity. Particle velocities and rotation rates are obtained by a spatial average of the fluid velocity and vorticity over the volume of fluid occupied by the particle, based on the spherical Gaussian envelopes Eq. (4) as

$$\mathbf{V}^{(n)}(t) = \int \mathbf{u}(\mathbf{x},t)\Delta[\mathbf{x} - \mathbf{Y}^{(n)}(t)]d^3\mathbf{x} \tag{8}$$

$$\boldsymbol{\omega}^{(n)}(t) = \frac{1}{2}\int \nabla \times \mathbf{u}(\mathbf{x},t)\Delta'[\mathbf{x} - \mathbf{Y}^{(n)}(t)]d^3\mathbf{x} \tag{9}$$

From this the trajectory of each spherical particle is computed as

$$\frac{d\mathbf{Y}^{(n)}}{dt} = \mathbf{V}^{(n)}(t) \tag{10}$$

In a Stokes flow, FCM gives exact results for the drag force on an isolated particle as well as the torque on a rotating sphere or the stresslet for a spherical particle in a uniform straining flow [19,20]. The response to a single force monopole captures both the usual Stokeslet and the associated degenerate force quadrupole needed to represent the flow past an isolated sphere. Even though boundary conditions are not imposed on the particle surface and only the constraints Eqs. (7)–(9) are imposed, the flow field is generally a good approximation at distances greater than 25–50% of the particle radius from the particle surface. Similarly, the hydrodynamic interaction of a pair of particles is well represented when the gap between the particles is larger than 25% of the radius, or 50% for the specific case of particles moving toward each other their line of centers where lubrication forces are then an issue [21].

The effects of finite fluid and particle inertia are well represented by the FCM scheme under low, but finite Reynolds numbers. This has been tested by comparisons with experiments for sedimenting particles [22] and against full direct numerical simulations for a variety of flows including particles in wall-bounded shear flows [23–25]. For flow past a fixed sphere, it has been verified so far that the drag forces and flow structure agree well with full direct numerical simulations at particle Reynolds numbers up to 12 [25]. FCM also gives good estimates for the lift forces on particles near a wall in a parallel shear flow, including situations involving a pair of interacting particles [26]. The computational effort for FCM as compared to direct numerical simulations for particulate flows is discussed by [23,24].

The Navier–Stokes Eqs. (1) and (2) are solved for a periodic cubic domain, large compared to the size of the particles and the typical scale of the aggregate. A Fourier pseudo-spectral representation is used for the flow field and a standard Fourier collocation scheme. Second-order time accuracy is achieved by using an Adams–Bashforth scheme for both the fluid and the particle motions. Simulations are carried out on both 64^3 and 128^3 grids. Typically 5–6 grid points per particle diameter are needed to ensure that the Gaussian force envelope Eq. (4) is resolved and that the body force distributions Eq. (3) are accurately represented, without aliasing errors.

2.2 Magnetic Forces. We now consider the effect of the magnetic field on the particles and the conditions relevant to the experiments [15] used here to motivate the simulations. The magnetized disks are of uniform size with diameter in the range of 1–2 mm and the final aggregated clusters are 10 mm or less in diameter. At 2–4 cm above the free surface a large permanent bar magnet is suspended, with horizontal dimensions 5.6 cm by 4 cm, which is then rotated rapidly at rates variously between ~200 rpm and 1200 rpm. On the free surface, the magnitude of the magnetic field has a maximum at the axis of rotation and the magnetic field is aligned with the long axis of the bar magnet. Locally, the magnet exerts a torque on a magnetized disk equal to $\mathbf{m}\times\mathbf{B}$ where $\mathbf{B}$ is the local magnetic flux density of the bar magnet and $\mathbf{m}$ is the fixed dipole moment of the disk [27]. Provided the two are aligned the torque is zero but any misalignment will generate a significant torque tending to bring the two back into alignment. The torque is more than sufficient to overcome the viscous resistance to rotation and so the disks rotate in synchrony with the bar magnet.

The bar magnet also exerts a force on each disk $\mathbf{m}\cdot\nabla\mathbf{B}$ associated with the gradient of the magnetic field. As the dipole moment is aligned with the bar magnet and the magnetic flux density is diminishing away from the axis of rotation, the force is directed toward the axis at all times. The magnitude of the force fluctuates as the magnet is rotated but as the rotation rate is much larger than the precession rate of the cluster of disks, the force may be represented by a time-averaged, constant force. The magnetic force also varies with radial distance from the axis of rotation. If the dimensions of the magnet were very large, we would expect a linear variation in the gradient of the flux density $\nabla\mathbf{B}$ with radial distance and so too of the magnetic force. This is only partially true and an alternative is to assume a locally uniform value of the flux gradient density over a limited range of distances from the axis. Both representations were used by Grzybowski et al. [15]. In the present simulations, we consider both a constant and a linearly varying radial magnetic force directed towards the axis of rotation to set $\mathbf{F}_{\text{ext}}$. The magnetic forces between individual disks, due to their dipole moments, are negligible by comparison.

The present numerical analogy of the experiments is composed of neutrally buoyant particles instead of disks floating at a liquid/air interface. It has been argued in the physical analysis of the self-assembly dynamics that capillary effects related to particle-interface interactions have no role. The net effect is only to prevent disks from settling under gravity in the fluid layer. We agree with such an analysis and set the density ratio $m_P/m_F=1$ throughout all the simulations. The hydrodynamic interactions are obtained by the force coupling method and these drive the Lagrangian motion of the spherical particles. The magnetic torque $\mathbf{T}_{\text{ext}}$ acting on each particle is fixed so that the angular velocity for a single particle matches the rotation of the magnetic field and that the corresponding rotational Reynolds numbers match.

3 Flow Interactions of Isolated Particles

The dynamics of self-assembly for particles under rotation and magnetic attraction are closely related to the hydrodynamic interactions of spinning spheres. In this section, we consider the flow generated by a single spinning sphere and the fluid forces acting on a pair of particles. We first compute the fluid velocity induced by a single isolated particle rotating around the fixed z axis passing through the center of the sphere. The particle radius is a and the rotation rate about the axis is ω. All quantities are made dimensionless using these two characteristic scales. In Fig. 2, we compare the radial profile of the azimuthal velocity, u_ϕ in the equatorial plane $\theta=\pi/2$ specified in terms of spherical polar coordinates (r,θ,φ). Simulations using the Stokes equations, at zero Reynolds number, are in good agreement with the analytic profile $u_\phi=a^3\omega/r^2$, for $r\geqslant a$. Close to the sphere surface at $r/a=1$ the discrepancy is slightly greater but at distances larger than $r/a=1.5$, good agreement is achieved. The FCM profile is smoothly varying and peaks inside the sphere volume. As the particle Reynolds number $\text{Re}_\omega=\omega a^2/\nu$ for the rotation is increased, where ν is the kinematic viscosity μ/ρ, the FCM results (with both torque and stresslet terms) indicate that there is little change in the azimuthal velocity profile. At $\text{Re}_\omega=8$, the profile is essentially identical to that at zero Reynolds number. At higher Reynolds number it is known that a boundary layer structure eventually develops [28] and the variation in azimuthal velocity with θ also changes.

In using the force coupling method here, the particle rotation rate $\boldsymbol{\omega}$ is determined from the simulation, using Eq. (9), in response to the flow generated by a prescribed torque $\mathbf{T}_{\text{ext}}$. We initially imposed $T_{\text{ext}}=8\pi\mu a^3\omega$, based on the reference set of scales and the viscous torque in Stokes flow [29], and then varied the fluid viscosity μ to achieve the required particle rotation Reynolds number. The relation between the torque and the angular velocity has been thoroughly investigated in the literature. The nondimensional torque $M=2T_{\text{ext}}/(\rho a^5\omega^2)$ varies with the Reynolds number

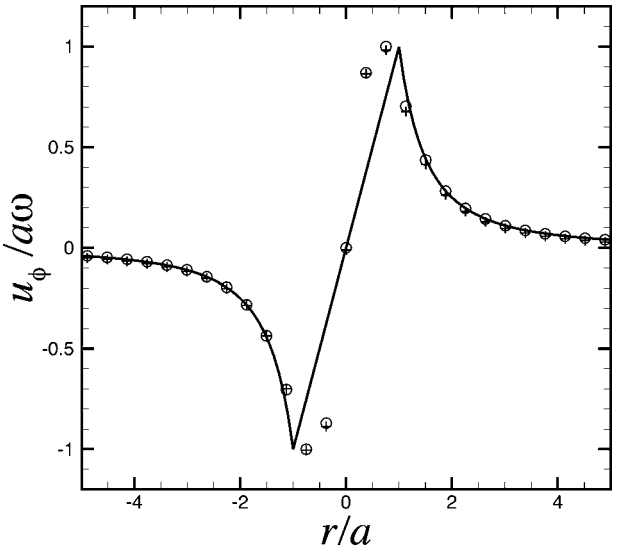

Fig. 2 Profile of the azimuthal velocity u_φ in the equatorial plane: Stokes flow (solid line); force coupling method–Stokes flow (open circles); force coupling method –Re_ω=8(+)

Re_ω. Experiments carried out by Sawatzki [30] are in good agreement with Lamb's result $M=16\pi/Re_\omega$ for Stokes flow [29] provided Re_ω is less than 3. This is confirmed by the numerical simulations of Dennis et al. [31]. When Re_ω becomes finite, the empirical relation $M=16\pi(1+f(Re_\omega))/Re_\omega$ is more appropriate. In the range $0\leqslant Re_\omega\leqslant 10$, the correction term $f(Re_\omega)$ remains small, less than 0.075, and the results for M obtained by Dennis et al. [31] agree well with the asymptotic approximations due to Bickley [32] and Takagi [33]. Results for M as a function of Re_ω obtained from the FCM simulations are shown in Fig. 3, where we include results with both torque and stresslet terms (FCM-TS) or with just a torque term (FCM-T). The stresslet term has a significant effect in improving the estimate of M as a function of Re_ω and improves the representation of the flow. At Re_ω=8, the expected value of $[1+f(Re_\omega)]$ is 1.050 while the results for FCM-TS give 1.016. The results are closer at lower Reynolds numbers.

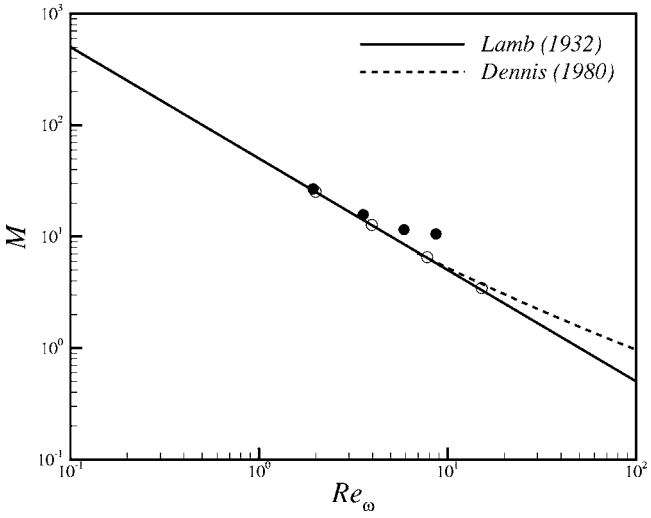

Fig. 3 Nondimensional torque coefficient M against Reynolds number Re_ω: solid line, Lamb's theory (Stokes flow); dashed line, correlation from the experiments of Sawatzki [30] and simulations of Dennis et al. [31]; filled circles, FCM-T results; open circles, FCM-TS results

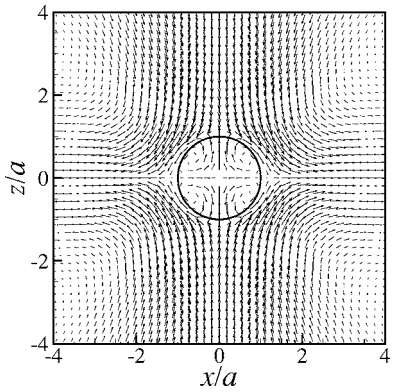

Fig. 4 Secondary flow in *x*, *z* plane for sphere spinning about the *z* axis at Re_ω=2

Overall, the estimate from Stokes flow provides a good approximation for the torque and the FCM results tend to underestimate the increase in torque. The working range for the experiments [15] is $0<Re_\omega<4$.

At finite Reynolds number a secondary, meridional circulation develops with an inflow at the poles and outflow near the equator. Figure 4 shows the simulation results for Re_ω=2 with rotation about the z axis. We have included the volume inside the particle to illustrate the internal circulation and the location of the stagnation points. The secondary flow can be approximately estimated by a regular perturbation expansion at low Reynolds number. Following Bickley [32], the three velocity components in terms of spherical polar coordinates are

$$u_r=-\frac{\omega a^3}{8r^2}(3\cos^2\theta-1)\left(1-\frac{a}{r}\right)^2 Re_\omega$$

$$u_\theta=\frac{\omega a^4}{4r^3}\left(1-\frac{a}{r}\right)\sin\theta\cos\theta\, Re_\omega$$

$$u_\phi=\frac{\omega a^3}{r^2}\sin\theta+O(Re_\omega^2) \tag{11}$$

This result illustrates the low Reynolds number stresslet component of the radial velocity in the plane $\theta=\pi/2$, where u_r varies asymptotically as $(\omega a^3/8r^2)Re_\omega$.

If in addition to rotation, a sphere is moving with a translational velocity U through still fluid there will be both a drag force and a lift force. The lift is orthogonal to both the linear velocity and the angular velocity. Rubinow and Keller [34] have estimated these forces for small, but finite Reynolds number using an Oseen representation for the far field flow. The drag coefficient is equal to the usual Oseen prediction, $C_D=24(1+3Re/16)/Re$, where the Reynolds number $Re=2aU/\nu$ and the lift coefficient is $C_L=3/4$. A force balance can be derived for steady motion with velocity $\mathbf{V}$

$$\mathbf{F}_{ext}=6\pi\mu a\mathbf{V}\left(1+\frac{3}{16}Re\right)+\frac{3}{4}m_F\mathbf{V}\times\boldsymbol{\omega} \tag{12}$$

while the particle is driven by a constant external force and $Re\ll 1$. Similarly for a sphere translating relative to a flow with a uniform shear, there is also a lift force. This is again an effect of finite Reynolds number and has been estimated by Saffman [35,36] to first order in Re. Extensive comparisons with FCM and full direct numerical simulations [23,25] have shown that the present simulation methods accurately capture these lift forces for low to moderate Reynolds numbers.

We now consider the motion of a pair of co-planar particles, each subject to a constant torque and co-rotating with an angular velocity ω. In a Stokes flow, at zero Reynolds number, the particles will follow a circular path moving in response to the flow

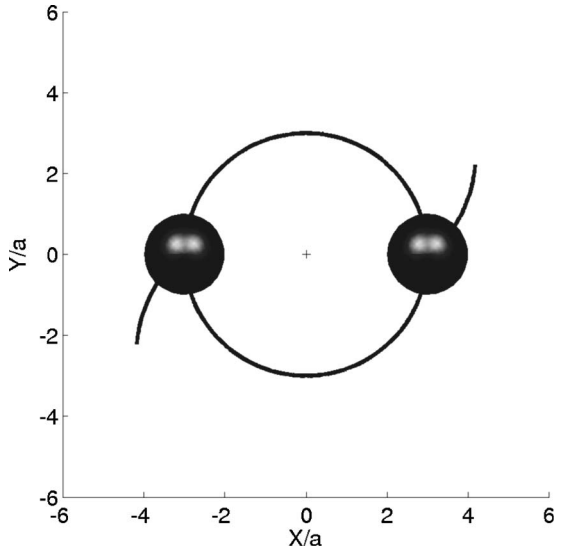

Fig. 5 Trajectories of two spinning particles without magnetic attraction: closed circular trajectories (Stokes flow); open trajectories (low, but finite Reynolds number)

generated by the other particle. There is no repulsion force between the particles and the radius of the circular path R does not change. This is shown by the closed path trajectories in Fig. 5 which are computed for zero Reynolds number. This agrees with the properties of linearity and reversibility for Stokes flows. When including low, but finite fluid inertia ($\mathrm{Re}_\omega=2$) in the simulation, we see that the particles repel each other. The particles follow open trajectories while the center to center distance increases steadily. The repelling behavior of spinning particles is clearly an effect of fluid inertia. If the particles are counter-rotating under the action of equal and opposite torques then in a Stokes flow the particles move in parallel with a constant velocity again in response to the flow induced by the other particle. Their separation distance $2R$ again remains constant.

This situation may be thought (as in the original discussions of the experiments) to give rise to a lift force at finite Reynolds number, either due to the shear flow (Saffman lift force) of the induced fluid motion or the rotation of the particles (Rubinow–Keller lift force). If this were the case then corotating particles would repel and counter-rotating particles would attract at finite Reynolds number. A simulation, similar to that shown in Fig. 5, with counter-rotating particles demonstrates that there is a repulsion not an attraction between the particles. Both the Rubinow–Keller lift force due to rotation and the Saffman lift force due to a local mean shear require a relative motion between the particle and the ambient fluid. Specifically, some wake region must develop behind each particle. The particles here are neutrally buoyant and their translational motion is due to the motion of the surrounding fluid, induced by the spinning particles. No such wake region will develop.

The flow structure for a pair of corotating particles is shown in Fig. 6. The particles are spinning about axes parallel to the z axis at $\mathrm{Re}_\omega=2$. They are subject to a fixed force of attraction that in the stationary state keeps them at a constant separation distance and the particles move in a circular path in the x,y plane. The distance between the particle centers, $2R$ is approximately $6a$. The secondary flow effect is clearly evident and the radial outflow in their common plane tends to push the particles apart. The flow structure is similar if the particles are counter-rotating, i.e., there is a common radial outflow for each particle.

We have computed the hydrodynamic repulsion force between a pair of particles, at fixed Reynolds numbers Re_ω, as a function of the particle separation distance $2R$. In the simulations, a constant force of attraction is set and then the equilibrium distance is determined. The results are show in Fig. 7 for $\mathrm{Re}_\omega=0.25$, 2, and 8. The force is scaled as $F/\rho a^4\omega^2$. The results for $\mathrm{Re}_\omega=0.25$ and 2 are very similar for $R/a>2$. There is no simple power law for the variation with separation distance but the trend is not far from an R^{-3} dependence. At the higher Reynolds number, the decrease with R is less.

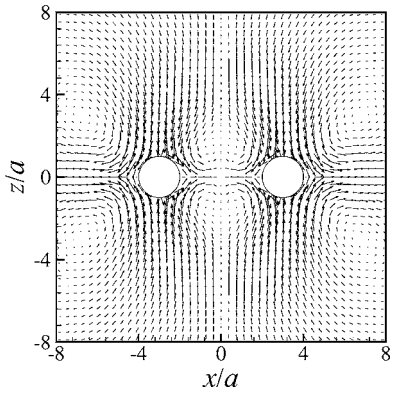

Fig. 6 Secondary flow for two spheres, spinning about axes parallel to the *z* axis, at $\mathrm{Re}_\omega=2$

The precession angular velocity Ω of the pair of particles can be theoretically predicted in Stokes flow by a linear summation of the velocity perturbations of each particle. Considering one particle of the aggregate, we can predict the azimuthal velocity induced by the rotation of the second particle as $u_\phi=\omega a^3/(2R)^2$. The angular frequency of the two particle system (precession velocity) is $\Omega=u_\phi/R$, and

$$\frac{\Omega}{\omega}=\frac{1}{4}\left[\frac{a}{R}\right]^3 \tag{13}$$

The relation strongly depends on the separation distance, varying as $1/R^3$. For an aggregate of three particles, following the same arguments we can derive

$$\frac{\Omega}{\omega}=\frac{1}{2\cos(\pi/6)}\left[\frac{a}{R}\right]^3 \tag{14}$$

Figure 8 summarizes the simulation results for a pair of particles. The results were obtained in the same way as in Fig. 7. It is important to note that the rotation rate of the aggregate Ω is typically one or two orders of magnitude lower than the reference angular frequency ω of the bar magnet. The above theoretical prediction based on Stokes flow is in good agreement with the

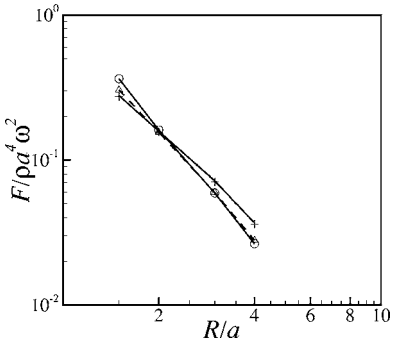

Fig. 7 Repulsion force *F* between two corotating particles against distance *R*, where 2*R* is the distance between particles. Results at $\mathrm{Re}_\omega=0.25$ (open circles), 2 (triangles), and 8 (cross)

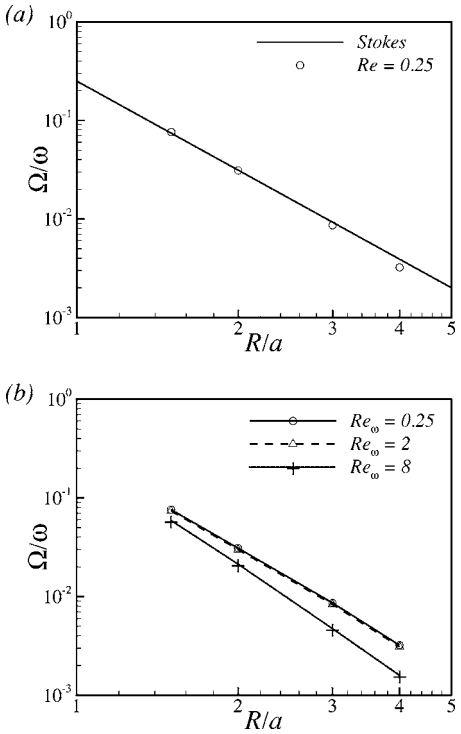

Fig. 8 Precession angular velocity Ω for a pair of corotating spheres against *R*: (*a*) comparison of results at Re_ω=0.25 with estimate from Stokes flow; and (*b*) comparison of results at Re_ω=0.25, 2, and 8

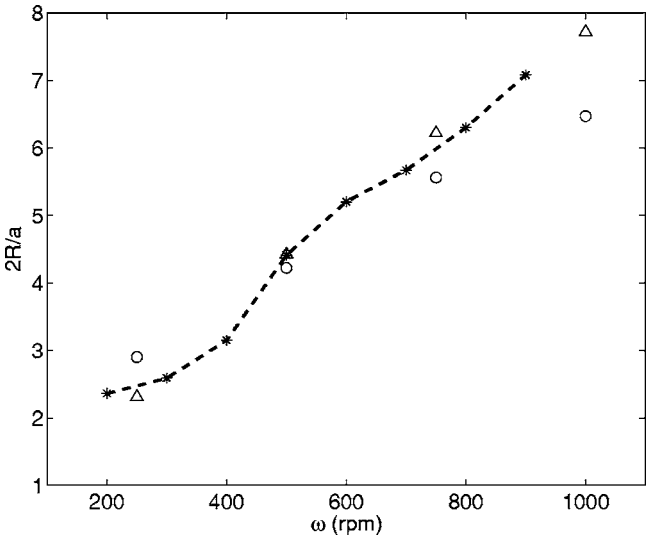

Fig. 9 Comparison of simulation results with experiments for the separation distance of the stable pattern (two particles) at different rotation rates ω: (stars) experiments of Grzybowski et al. [15] (dashed line is only a guide for the eye); (triangles) FCM results with a constant magnetic attraction force; (circles) FCM results with a linear magnetic attraction force

simulations at Re_ω=0.25 and 2 for smaller separation distances. At the higher Reynolds number, Re_ω=8, the decrease in Ω is more rapid with separation distance.

4 Self-Assembly of Rotating Particles

We now consider the motion of spinning particles that are also subject to a central attraction force due to the rotating magnetic field and make comparisons with the experiments [15]. Particles are initially seeded at random positions in the same plane (see Fig. 1) to correspond to the coplanar experimental conditions where disks were floating beneath a liquid–air interface. We do not force the particles to stay in the initial plane and the particles may move freely within the three-dimensional periodic domain. Throughout, a stable coplanar configuration of the aggregate is reached as self-assembly occurs. It is important to note that the typical size of the cluster of particles is small compared to the domain width (24 or 48 particle radii) and the periodic boundary conditions have been verified to have only a small effect on the overall dynamics.

4.1 Two Particle System. The simplest stable aggregate is composed of two particles, where the repelling hydrodynamic force is balanced by a centripetal force given by the magnetic attraction toward the rotation axis of the bar magnet. Note that stable does not mean fixed since the particles are spinning around their own axes, and they induce a disturbance flow leading to the precession of the aggregate itself. We consider both a constant value for the magnetic attracting force and a linearly varying force to compare with the experimental data [15]. In Fig. 9, the increasing separation distance between the two particles of the rotating aggregate depends on the angular frequency. With increasing rotation rate of the bar magnet, the magnitude of the flow associated with the spinning particles increases and so too the inertial repulsion force. The particles then move apart from each other giving larger separation distance $2R/a$. In order to set an appropriate magnitude for the magnetic attraction force the result at ω =500 rpm, which corresponds to Re_ω=2, was used as reference point. The separation distance $2R/a$ is equal to 4.42 in this case.

There is good general agreement between the experimental data and the results of the simulations over the entire range of angular frequency. The results with the constant value of the magnetic force, shown by the triangular symbols in the figure, are in better agreement to the experiments than those for the linearly varying magnetic force, shown by the open circles. Note that with a linearly varying force, the attraction is stronger for larger values of R while the hydrodynamic repulsion becomes weaker. As a result, the separation distance $2R$ is smaller for a high rotation rate and conversely larger at a low rotation rate. The largest distance between the particles is less than 8 particle radius which is much lower that the width of the simulation domain (24 particle radius).

4.2 Multiple Particle System. As the number N_B of particles involved in an aggregate is increased, the topology of the self-assembling cluster changes. From two to five particles, the aggregate is composed of one single shell without particle in its center. The particles are distributed evenly on the circular orbit described by each particle trajectory. When N_B equals six, seven, or eight particles, one particle is located in the center of the circular orbit of the rotating aggregate. If nine particles are initially seeded at random positions, the aggregate achieves a stable configuration composed of two shells: two inner particles rotating around the rotation axis of the bar magnet and an outer shell composed of seven particles following circular paths (see Fig. 10 for stable

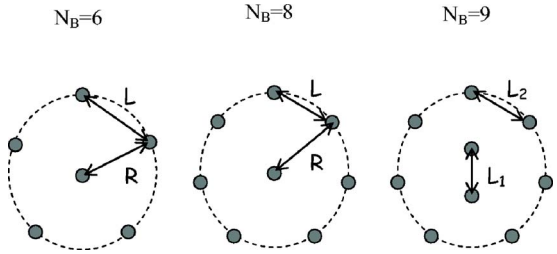

Fig. 10 Definition of length scales for a rotating aggregate

Table 1 Typical scales of a rotating aggregate (experiments, simulations)

$N_B=6$	$N_B=8$	$N_B=9$
$R/a=4.33$	$R/a=4.54$	$L_1/a=3.38$
$L/a=5.08$	$L/a=4.17$	$L_2/a=4.33$
$L/R=1.17$ (simulation)	$L/R=0.91$ (simulation)	$L_1/L_2=0.78$ (simulation)
$L/R=1.13$ (experiments)	$L/R=0.80$ (experiments)	$L_1/L_2=0.80$ (experiments)

configurations for $N=6$, 8, or 9). We checked the stability of these aggregate organizations by simulating the self-assembling transient from different initial random seeding. The particles always reach the same configuration as observed experimentally. At this point, we do not have a complete understanding of the selection mechanism for the aggregate patterns but the simulations show clearly that the FCM simulations are able to reproduce such complex dynamics.

In Table 1, the geometric parameters that define the aggregate pattern for $N=6$, 8, and 9 particles are given. These are compared with the experimental data and it can be seen that the agreement is more than qualitative for the cases $N=6$ and $N=9$. Our simulations overestimate slightly (13% error) the separation distance for a cluster composed of eight particles, as compared to the experiments. Full agreement is not to be expected because of the differences in the configuration of the experiments (disks) and the simulations (spheres). The values of R/a are all in a similar range and the results are similar whether a linearly varying or constant magnetic force is used. Figure 11 shows the flow field for a stable aggregate of seven particles, plotted for their common plane of motion.

For the particular values of $N=10$ and $N=12$, a polymorphism was observed in the experiments [16], whereby two different stable configurations of the particles can occur. Figure 12 shows the corresponding simulation results for ten particles at $\mathrm{Re}_\omega=2$. The two stable patterns have either seven or eight particles in the outer shell and correspondingly three or two particles nearer the center. For $N=12$, Fig. 13 shows that the stable patterns have either eight or nine particles in the outer shell. Both observations agree with the experiments. Starting from different, random initial positions of the particles it was seen in the experiments that the eight particles in the outer shell were more common for $N=10$ and the nine particles in the outer shell for $N=12$. The statistics varied somewhat with the rotation rate. We do not have sufficient data to estimate the relative frequency of each pattern but the results show a similar trend.

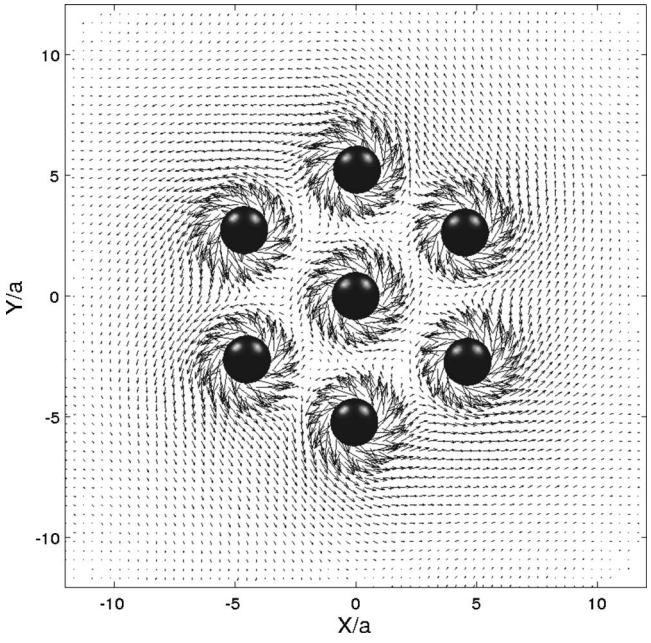

Fig. 11 Fluid velocity vectors for a stable aggregate of rotating spheres, $N=7$, at $\mathrm{Re}_\omega=2$. The aggregate precesses about the center particle in this common plane.

5 Discussion

In this paper, we give results from the numerical simulation of dynamic self-assembly of spinning particles. The key mechanism is the hydrodynamic repulsion between the particles that balances the magnetic attraction toward the center of the domain. Multibody hydrodynamic interactions are determined by numerical solutions of the Navier–Stokes equations combined with the force

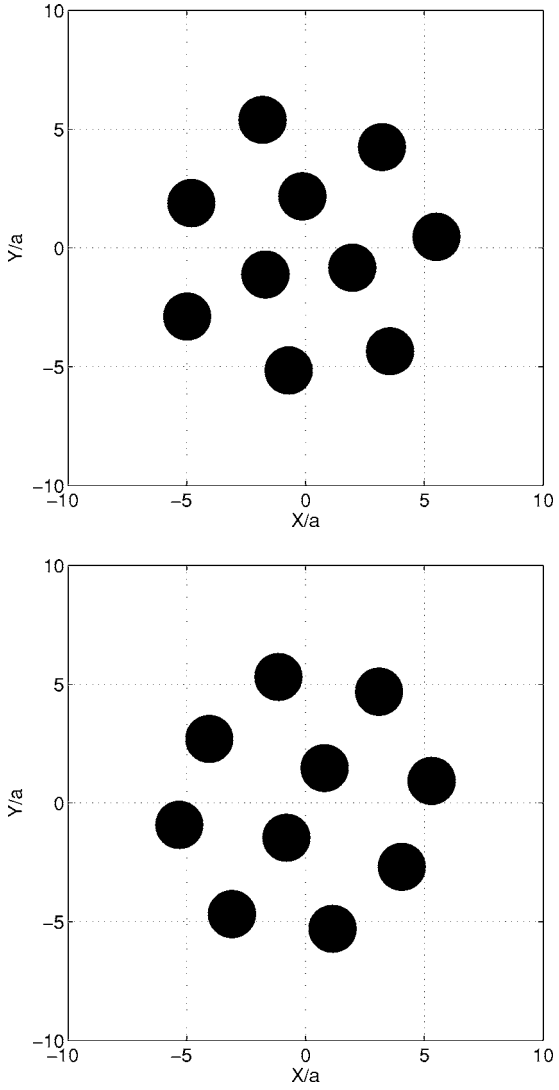

Fig. 12 Stable aggregation patterns for $N=10$ at $\mathrm{Re}_\omega=2$

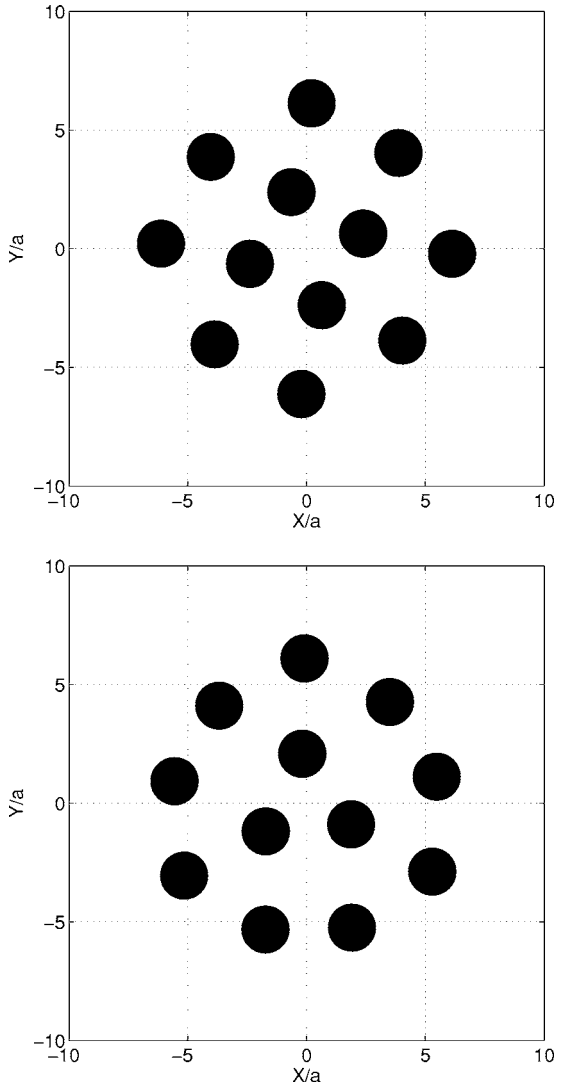

Fig. 13 Stable aggregation patterns for $N=12$ at $\mathrm{Re}_\omega=2$

coupling method as a representation for the interphase coupling between the fluid flow and the particles. The model is fully coupled in that particle rotations induce velocity perturbations in the flow that in turn drive the overall dynamics of the aggregate formation and govern the stability.

We simulate the formation of self-assembling aggregates composed of different numbers of particle. The configuration of two particles was compared to the reference experiments of Grzybowski et al. [15,16]. Our simulations on the evolution of the interparticle distance with the rotation rate of the bar magnet are in good agreement with the experiments carried out with spinning disks at a liquid–air interface. This demonstrates that the dynamics are purely related to hydrodynamic interactions and are not driven by interfacial phenomena. An important conclusion of our simulations is that the basic features are prescribed by low but finite Reynolds number dynamics and would not develop in the absence of fluid inertia. The repulsion force is Reynolds number dependent and the precession velocity is a function of the Reynolds number of the flow and the interparticle distance. When the number of particles is further increased, the arrangement of the particles displays symmetric patterns with one or more particles in the center surrounded by a rotating shell of equidistant particles. Polymorphism is observed too for groups of 10 or 12 particles.

Such tunable properties are highly desirable at microscales where the precise control of particle organization can drive the macroscopic properties of the equivalent medium. We may expect a high efficiency of mixing in a flow using such active microsystems, as indicated by Campbell and Grzybowski [37]. Although the effects depend on fluid inertia at finite Reynolds number, a low value of $\mathrm{Re}_\omega \sim 0.1$ would be sufficient to produce self-assembly. Such values are quite feasible in microflow systems at high rotation rates.

We have demonstrated that the source of the hydrodynamic repulsion force observed in the simulations and the experiments is the secondary flow generated by the spinning particles as opposed to lift forces. The variation of the force with separation distance, shown in Fig. 7, is consistent with the observations from the experiments. Grzybowski et al. [15] postulate scaling relations for the repulsion force assuming some form of lift force but conclude that straightforward estimates do not agree with the observed variations of the force with separation distance. By assuming a radial repulsion force that scales as r^{-3} [16] and suitable scaling coefficients, they were able to obtain a good correspondence between analytical model estimates and the experiments. In the present simulations, no such assumptions are required. Qualitatively, the secondary flow around each spinning particle will further produce a pressure force that will tend to support the particle at the free surface between the liquid and the air and the spinning particles could be viewed as roughly analogous to spinning hemispheres.

Finally, we note that there are several unresolved issues. The most important is that the FCM simulations tend to underpredict the strength of the secondary flow, although the spatial variation is approximately correct. Preliminary investigations have shown this to be the result of limited resolution of the flow near the surface of the sphere. The secondary flow is forced by pressure variations on the surface of the particle and is sensitive to the profile of u_ϕ. The differences between the exact solution and the FCM results shown in Fig. 2, while small, are significant for $1<r/a<1.5$. We are continuing to investigate this issue and improve the accuracy of the simulations.

Acknowledgment

The research was supported by the National Science Foundation under Grant No. CTS-0326702 and by CNRS under a PICS CNRS–USA collaborative program. Simulations were performed with the support of regional and national supercomputing centers Calmip, CINES/IDRIS. Findings and conclusions expressed here are those of the authors do not necessarily reflect the views of the funding agency. We are grateful to Professor Grzybowski of Northwestern University for discussion of the experiments.

References

[1] Stone, H. A., Stroock, A. D., and Ajdari, A., 2004, "Engineering Flows in Small Devices: Microfluidics toward a Lab-on-a-Chip," Annu. Rev. Fluid Mech., **36**, pp. 381–411.
[2] Stone, H. A., and Kim, S., 2001, "Microfluidics: Basic Issues, Applications, and Challenges," AIChE J., **47**(6), pp. 1250–1254.
[3] Nguyen, N.-T., and Wu, Z., 2005, "Micromixers-A Review," J. Micromech. Microeng., **15**, pp. R1–R15.
[4] Ottino, J. M., and Wiggins, S., 2004, "Introduction: Mixing in Microfluidics," Philos. Trans. R. Soc. London, Ser. A, **362**, pp. 923–935.
[5] Biswal, S. L., and Gast, A. P., 2004, "Micromixing with Linked Chains of Paramagnetic Particles," Anal. Chem., **76**, pp. 6448–6455.
[6] Terray, A., Oakley, J., and Marr, D. W., 2002, "Microfluidic Control Using Colliodal Devices," Science, **296**, pp. 1841–1843.
[7] Liu, D., Maxey, M. R., and Karniadakis, G. E., 2004, "Modeling and Optimization of Colloidal Micro-Pumps," J. Micromech. Microeng., **14**(4), pp. 567–575.
[8] Hayes, M. A., Polson, N. A., and Garcia, A. A., 2001, "Active Control of Dynamic Supraparticle Structures in Microchannels," Langmuir, **14**, pp. 2866–2871.
[9] Doyle, P. S., Bibette, J., Bancaud, A., and Viory, J.-L., 2002, "Self-Assembled Magnetic Matrices for DNA Separation Chips," Science, **295**, p. 2237.
[10] Promislow, J. H., Gast, A. P., and Fermigier, M., 1995, "Aggregation Kinetics of Paramagnetic Colloidal Particles," J. Chem. Phys., **102**, pp. 5492–5498.
[11] Climent, E., Maxey, M. R., and Karniadakis, G. E., 2004, "Dynamics of Self-Assembled Chaining in Magneto-Rheological Fluids," Langmuir, **20**, pp.

507–513.
[12] Liu, D., Maxey, M. R., and Karniadakis, G. E., 2005, "Simulations of Dynamic Self-Assembly of Paramagnetic Microspheres in Confined Microgeometries," J. Micromech. Microeng., **15**(12), pp. 2298–2308.
[13] Whitesides, G. M., and Grzybowski, B., 2002, "Self-Assembly at All Scales," Science, **295**, pp. 2418–2421.
[14] Grzybowski, B. A., Stone, H. A., and Whitesides, G. M., 2000, "Dynamic Self-Assembly of Magnetized, Millimeter-Sized Objects Rotating at a Liquid-Air Interface," Nature (London), **405**, pp. 1033–1036.
[15] Grzybowski, B. A., Jiang, X., Stone, H. A., and Whitesides, G. M., 2001, "Dynamic, Self-Assembled Aggregates of Magnetized, Millimeter-Sized Objects Rotating at the Liquid-Air Interface: Macroscopic, Two-Dimensional Classical Atoms and Molecules," Phys. Rev. E, **64**, 011603.
[16] Grzybowski, B. A., Stone, H. A., and Whitesides, G. M., 2002, "Dynamics of Self-Assembly of Magnetized Disks Rotating at the Liquid-Air Interface," Proc. Natl. Acad. Sci. U.S.A., **99**(7), pp. 4147–4151.
[17] Aref, H., 1983, "Integrable, Chaotic and Turbulent Vortex Motion in Two-Dimensional Flows," Annu. Rev. Fluid Mech., **15**, pp. 345–389.
[18] Campbell, L. J., and Ziff, M., 1979, "Vortex Patterns and Energies in a Rotating Superfluid," Phys. Rev. B, **20**(5), pp. 1886–1902.
[19] Maxey, M. R., and Patel, B. K., 2001, "Localized Force Representations for Particles Sedimenting in Stokes Flows," Int. J. Multiphase Flow, **27**, pp. 1603–1626.
[20] Lomholt, S., and Maxey, M. R., 2003, "Force-Coupling Method for Particulate Two-Phase Flow. Stokes Flow," J. Comput. Phys., **184**, pp. 381–405.
[21] Dance, S. L., and Maxey, M. R., 2003, "Incorporation of Lubrication Effects into the Force-Coupling Method for Particulate Two-phase Flow," J. Comput. Phys., **189**, pp. 212–238.
[22] Lomholt, S., Stenum, B., and Maxey, M. R., 2002, "Experimental Verification of the Force Coupling Method for Particulate Flows," Int. J. Multiphase Flow, **28**, pp. 225–246.
[23] Liu, D., Maxey, M. R., and Karniadakis, G. E., 2002, "A Fast Method for Particulate Microflows," J. Microelectromech. Syst., **11**, 691–702.
[24] Dong, S., Liu, D., Maxey, M. R., and Karniadakis, G. E., 2004, "Spectral Distributed Lagrange Multiplier Method: Algorithm and Benchmark Tests," J. Comput. Phys., **195**, pp. 695–717.
[25] Liu, D., 2004, "Spectral Element/Force Coupling Method: Application to Colloidal Micro-Devices and Self-Assembled Particle Structures in Three-Dimensional Domains," Ph.D. thesis, Brown University, Providence, RI.
[26] Maxey, M. R., Liu, D., Dong, S., and Karniadakis, G. E., 2006, "New Advances in Force-Coupling Method: From Micro to Macro," *Proceedings of the IUTAM Symposium on Computational Multiphase Flow*, S. Balachandar and A. Prosperetti, eds, Springer, New York, pp. 237–246.
[27] Jackson, J. D., 1999, *Classical Electrodynamics*, 3rd ed., Wiley, New York.
[28] Howarth, L., 1951, "Note on the Boundary Layer on a Rotating Sphere," Philos. Mag., **42**, pp. 1308–1315.
[29] Lamb, H., 1932, *Hydrodynamics*, Cambridge University Press, Cambridge, UK, pp. 558–559.
[30] Sawatzki, O., 1970, "Flow Field around a Rotating Sphere," Acta Mech., **9**, pp. 159–214.
[31] Dennis, S. C. R., Singh, S. N., and Ingham, D. B., 1980, "The Steady Flow due to a Rotating Sphere at Low and Moderate Reynolds Number," J. Fluid Mech., **101**, pp. 257–279.
[32] Bickley, W. G., 1938, "The Secondary Flow due to a Sphere Rotating in a Viscous Liquid," Philos. Mag., **25**, pp. 746–752.
[33] Takagi, H., 1977, "Viscous Flow Induced by Slow Rotation of a Sphere," J. Phys. Soc. Jpn., **42**(1), pp. 319–325.
[34] Rubinow, S. I., and Keller, J. B., 1961, "The Transverse Force on a Spinning Sphere Moving in a Viscous Fluid," J. Fluid Mech., **11**, pp. 447–459.
[35] Saffman, P. G., 1965, "The Lift on a Small Sphere in a Slow Shear Flow," J. Fluid Mech., **22**, pp. 385–400.
[36] Saffman, P. G., 1968, "Corrigendum: The Lift on a Small Sphere in a Slow Shear Flow," J. Fluid Mech., **31**, pp. 624.
[37] Campbell, C. J., and Grzybowski, B. A., 2004, "Microfluidic Mixers: From Microfabricated to Self-Assembled Devices," Philos. Trans. R. Soc. London, Ser. A, **362**, pp. 1069–1086.